

---

# Spherical Strong-Shock Generation for Shock-Ignition Inertial Fusion

## Introduction

Shock ignition (SI)<sup>1–5</sup> is an advanced concept in inertial confinement fusion (ICF)<sup>6</sup> that is very promising and has the potential to provide significantly higher gains than conventional hot-spot ignition.<sup>7</sup> SI is a two-step process where the fuel compression and ignition phases are separated by applying a highly shaped laser pulse with a duration of several nanoseconds. The concept of separating the compression and ignition phases has already been suggested by Shcherbakov,<sup>8</sup> but no detailed target design was presented. First, a cryogenic deuterium–tritium fuel shell is imploded to a high areal density with a low implosion velocity by a nanosecond laser driver; then a strong shock wave is launched at the end of the laser pulse that initiates ignition in the center of the compressed shell. A spherically converging shock wave is launched into the imploding shell by an abrupt increase in the power at the end of the laser pulse, producing an intensity spike of  $>5 \times 10^{15}$  W/cm<sup>2</sup>. The shock gains strength while propagating through the converging shell and is timed so that it meets the rebounded shock from the target center inside the shell close to the inner surface. This shock collision creates new shock waves; one of them propagates back to the capsule center, enhancing the piston action on the hot spot, and triggers ignition. Because SI implosions occur at a much lower velocity than in hot-spot ignition, significantly more mass can be assembled for the same laser energy, leading to higher gain if the fuel assembly can be ignited. The energy to achieve ignition is, according to simulations,<sup>1,4</sup> lower for SI than for hot-spot ignition. Two-dimensional (2-D) simulations<sup>9</sup> have also shown that SI targets are more resilient against hydrodynamic instabilities than hot-spot–ignition targets. The current status and the physics issues of the SI concept are reviewed in two articles that recently appeared in *Nuclear Fusion*.<sup>5,10</sup>

A critical component for SI is the strength of the ignitor shock, which depends on the energy coupling of the spike pulse. The laser-energy coupling into the target is not well understood at high-spike laser intensities. The inverse bremsstrahlung absorption, which is the main laser-energy absorption mechanism in ICF, significantly decreases in efficiency with higher intensities above  $10^{15}$  W/cm<sup>2</sup> (Ref. 11). For laser

intensities of up to  $10^{15}$  W/cm<sup>2</sup>, the absorption is in the regime of classical inverse bremsstrahlung absorption and the ablation pressure scales with the incident intensity according to  $P_{\text{abl}}(\text{Mbar}) \approx 57(\eta_{\text{abs}} I_{15} / \lambda_{\mu\text{m}})^{2/3}$  (Ref. 11), where  $\eta_{\text{abs}}$  is the laser-energy absorption fraction,  $I_{15}$  is the laser intensity in units of  $10^{15}$  W/cm<sup>2</sup>, and  $\lambda_{\mu\text{m}}$  is the laser wavelength in  $\mu\text{m}$ . One key issue for SI is to demonstrate that the spike pulse can generate a minimum ablation pressure of  $\sim 300$  Mbar (Refs. 4 and 12). If the classical model is used for extrapolation, absorbed laser intensities of at least  $\sim 4 \times 10^{15}$  W/cm<sup>2</sup> are required to launch sufficiently strong shocks on the target surface. Another critical issue is that laser–plasma instabilities play an important role in the high-intensity range. Laser–plasma instabilities<sup>13</sup> such as stimulated Brillouin scattering (SBS),<sup>14,15</sup> stimulated Raman scattering (SRS),<sup>16</sup> and the two-plasmon–decay (TPD) instability<sup>17,18</sup> are of concern in an ignition target design for two reasons: The instabilities generate energetic electrons that might preheat the shell, thereby reducing the final core compression; they also might increase the back-reflection of the laser light from the target, further degrading the laser–energy coupling to the capsule.

The physics of laser-spike absorption, ablation pressure generation, and hot-electron production are the major unknowns in the SI concept. Dedicated experiments must test the scaling of ablation pressure with spike intensity at SI-relevant laser intensities since there are currently insufficient experimental data at these high intensities. Only a few experiments have been performed to study laser-driven shocks in an intensity regime that is relevant for shock ignition.<sup>19–21</sup> These experiments utilized planar targets, however, that severely limit the attainable ablation pressure because of lateral heat losses from the laser spot. A spherical geometry is more relevant for SI and would minimize lateral heat losses, leading to higher pressures. Experiments on Laboratoire Pour L'Utilisation Des Lasers Intenses (LULI)<sup>19</sup> and OMEGA<sup>20</sup> used optical diagnostics to measure the shock-propagation velocity in a planar quartz witness sample layer. The shock breakout time at the target's rear surface was used as a metric to infer the peak ablation pressure on the laser-interaction side by comparing

the breakout time to predictions from 2-D radiation–hydrodynamic simulations. Peak ablation pressures of  $\sim 40$  Mbar were reached on LULI with  $0.53\text{-}\mu\text{m}$ -wavelength laser light at an intensity of  $\sim 1 \times 10^{15}$  W/cm<sup>2</sup> and  $\sim 75$  Mbar on OMEGA with  $0.35\text{-}\mu\text{m}$ -wavelength laser light and an absorbed intensity of  $1.2 \times 10^{15}$  W/cm<sup>2</sup>. Experiments at the Prague Asterix Laser Facility used the measured self-emission of the shock after breakout to infer shock pressures of up to 90 Mbar for intensities  $< 10^{16}$  W/cm<sup>2</sup> and a  $0.43\text{-}\mu\text{m}$  wavelength (Ref. 21). Recent OMEGA experiments have been more relevant to SI in terms of utilizing a spherical geometry and higher laser intensities. The experiments used solid plastic spheres that were irradiated by the OMEGA laser at intensities well above  $10^{15}$  W/cm<sup>2</sup>. An important finding was that the ablation pressure scales stronger than linearly with the laser intensity,<sup>22</sup> in contrast to what is expected from the classical model. Copious amounts of hot electrons are generated at incident laser intensities of  $> 3 \times 10^{15}$  W/cm<sup>2</sup> because of laser–plasma instabilities, which significantly enhance the pressure.

In this article we demonstrate the generation of ablation pressures of up to  $\sim 400$  Mbar in spherical strong-shock (SSS) experiments on the OMEGA laser, which is an important milestone for the SI concept. The demonstration of ablation pressures exceeding 300 Mbar is crucial to developing a robust SI target design for the National Ignition Facility (NIF).<sup>23</sup> The SSS experiments investigate the strength of the ablation pressure and the hot-electron production with overlapping incident beam laser intensities of  $\sim 2$  to  $6 \times 10^{15}$  W/cm<sup>2</sup>. The primary observable from these experiments is the timing of the x-ray flash from shock convergence in the center of a solid plastic target. This information is used in radiation–hydrodynamic simulations that are constrained by the experimental results to infer the ablation and shock pressures. The convergent geometry causes a large enhancement of the shock strength in the center of the solid target,<sup>24</sup> achieving multi-Gbar levels. The results are therefore also relevant to the development of a direct-drive platform to study material properties at Gbar pressures. Similar experiments have been proposed in indirect drive on the NIF to measure the equation of state and opacities of matter at Gbar pressures.<sup>25</sup>

This article is organized as follows: (1) The experimental setup, which includes a description of the target, the laser conditions, and the diagnostics is presented. (2) The experimental results from the x-ray emission, the hot-electron characterization, and the laser backscattering are described. (3) Radiation–hydrodynamic simulations are used to infer the ablation and shock pressures. (4) Finally, we conclude with a

discussion and an extrapolation of the ablation pressure for the NIF target design.

### Experimental Setup

Figure 14.1 shows a schematic of the experimental strong-shock platform. The 60 UV beams ( $0.351\text{-}\mu\text{m}$  wavelength) from the OMEGA laser<sup>26</sup> are focused to a high intensity (at an overlapping beam intensity of  $\sim 6 \times 10^{15}$  W/cm<sup>2</sup>) on the surface of a solid target to launch a spherical shock wave that converges in the center, heating a small volume ( $< 10\text{-}\mu\text{m}$  radius) to temperatures of several hundred electron volts (eV). At the time of shock convergence, a short burst of x rays emitted from the target is detected with an x-ray framing camera (XRFC)<sup>27</sup> and a streaked x-ray spectrometer (SXS).<sup>28</sup> The hot electrons are characterized from the measured hard x-ray bremsstrahlung emission. The absorbed laser power is measured and laser backscatter diagnostics characterize spectrally and temporally resolved optical emission generated by laser–plasma instabilities.

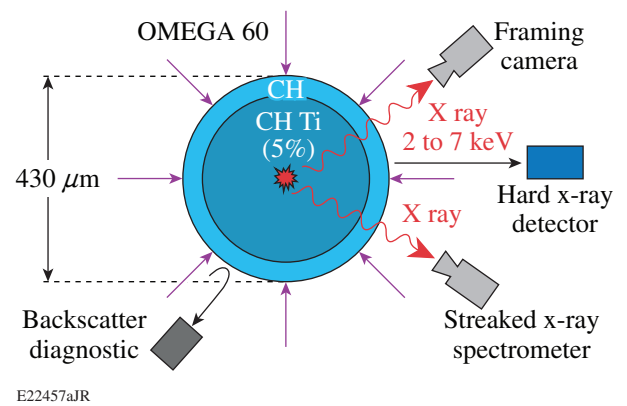


Figure 14.1.41

Schematic of the experimental OMEGA platform that is used to study the generation of strong shocks and the hot-electron production at shock-ignition–relevant laser intensities. A spherical shock wave is generated in solid targets, which converges in the center, producing a short burst of x rays that is detected with a framing camera and a streaked spectrometer. The hot electrons are characterized from the measured hard x-ray bremsstrahlung emission. The scattered laser light is measured temporally and spectrally resolved at different locations around the target to infer information on the laser–plasma instabilities and the total amount of absorbed laser energy.

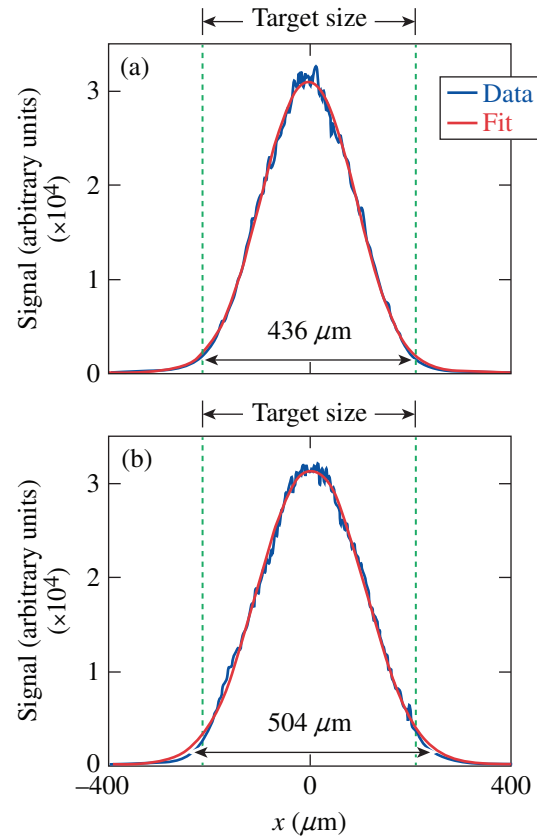
#### 1. Targets

The solid targets that were used comprised an outer 35- or  $50\text{-}\mu\text{m}$ -thick pure plastic (CH) ablator and an inner CH core doped with titanium with an atomic concentration of 5%. These targets, fabricated and characterized by General Atomics, had an outer diameter of 415 to  $600\text{ }\mu\text{m}$ . The sphericity ( $\Delta r/r$ ) of the

targets was better than 0.5%. The heated plasma in the target center emitted continuum bremsstrahlung and line emission from the dopant material. Simulations were performed with different doping materials and doping concentrations to optimize the yield from ionic line emission. The strongest line emission was calculated for doping concentrations of  $\sim 0.1\%$  atomic density with Ti. Because of manufacturing limitations, the doping concentration turned out to be 5% in the fabricated target, significantly higher than requested, which resulted in a considerable reabsorption of the emission from the center in the colder outer parts of the target. The opacity of the target might be an issue in interpreting the magnitude of the x-ray signal emitted by the central hot spot. Since the primary observable for determining the ablation pressure is the time of appearance of the x-ray flash, the opacity does not affect the data interpretation as long as the signal is strong enough to be measured, which was the case in our experiment. In addition, the 35- or 50- $\mu\text{m}$ -thick undoped outer CH layer ensures that any detected line emission originates in the target interior rather than the hot corona since simulations predict that only  $\sim 12\ \mu\text{m}$  of CH is ablated away during the laser interaction.

## 2. Laser Focus and Laser Pulse Shapes

The foci of the laser beams match the size of the smallest solid target. The 60 OMEGA beams were equipped with a mix of small-spot phase plates. Forty-three beams were equipped with IDI-300 phase plates developed for indirect-drive experiments,<sup>29</sup> 13 beams with ESG10-300, two beams with 100- $\mu\text{m}$ , and two beams with 200- $\mu\text{m}$  phase plates. The IDI-300 and ESG10-300 are elliptical phase plates, while the 100- $\mu\text{m}$  and 200- $\mu\text{m}$  phase plates provide small circular spots. While it is desirable to use a single type of phase plate, only 43 IDI-300's are available on the OMEGA Laser System. The complication of using a variety of small phase plates has a negligible effect on the primary observable. The elliptical phase plates were orientated such that the minor axis of the focus was aligned along the splitting direction of the birefringent optical wedges<sup>30</sup> to produce less-elliptical focal spots. Figure 141.42(a) shows a lineout through the minor axis of the elliptical focus of one of the laser beams equipped with an IDI-300 phase plate; Fig. 141.42(b) shows a lineout through the major axis. Polarization smoothing<sup>30</sup> and smoothing by spectral dispersion (SSD)<sup>31</sup> were applied to the beam. The far-field intensity distribution was measured using the ultraviolet (UV) equivalent-target-plane diagnostic.<sup>32</sup> Both lineouts are well fitted with super-Gaussian profiles having an order of  $n = 2.15 \pm 0.05$  and radii of  $218 \pm 5\ \mu\text{m}$  along the minor axis and  $252 \pm 7\ \mu\text{m}$  along the major axis (see Fig. 141.42). The radii correspond to the 5% point of the maximum intensity. Similar measurements were performed with SSD turned off,



E22458bJR

Figure 141.42

Lineouts through the (a) minor and (b) major axis of the elliptical focus of one of the laser beams. The beam was equipped with an IDI-300 phase plate and polarization rotator and used smoothing by spectral dispersion.

while retaining polarization smoothing, which resulted in a smaller spot. In this case, the fitting resulted in profiles with super-Gaussian orders and radii of  $n = 1.9 \pm 0.1$  and  $211 \pm 10\ \mu\text{m}$  along the major axis and  $n = 4.0 \pm 0.3$  and  $180 \pm 5\ \mu\text{m}$  along the minor axis, respectively. The spots are smaller when SSD is turned off, resulting in a higher single-beam intensity but similar average intensity when overlapping all 60 beams. Single beams without SSD contain significantly more nonuniformity, while turning on SSD reduces the single-beam uniformity  $\sigma_{\text{rms}}$  by a factor of  $\sim 8$  (Ref. 30). The ESG10-300 phase plates produce slightly less elliptical and smaller spots compared to the IDI-300 phase plates with  $n = 1.42 \pm 0.05$  and radii of  $169 \pm 5\ \mu\text{m}$  and  $179 \pm 5\ \mu\text{m}$ . The spot of the 200- $\mu\text{m}$  phase plate is round with  $n = 2.17 \pm 0.05$  and a radius of  $125 \pm 5\ \mu\text{m}$ . No data are available for the 100- $\mu\text{m}$  phase plate but it is expected that it produces a slightly smaller spot than the 200- $\mu\text{m}$  phase plate. No data are available for the spots for the ESG10-300, 200- $\mu\text{m}$ , and 100- $\mu\text{m}$  phase plates when SSD is turned off. A summary of the fitting results can be found in Table 141.III.

Table 141.III: Summary of the fitting results through the major and minor axes of the elliptical focus profiles of the different phase plates used in the experiment. The super-Gaussian orders and radii along the major axis and the minor axis are provided.

Phase plate	With SSD modulation				Without SSD modulation			
	$n_1$	$n_2$	$r_1$ ( $\mu\text{m}$ )	$r_2$ ( $\mu\text{m}$ )	$n_1$	$n_2$	$r_1$ ( $\mu\text{m}$ )	$r_2$ ( $\mu\text{m}$ )
IDI-300	2.14	2.15	218	252	4.0	1.9	180	211
ESG10-300	1.43	1.40	169	179	No data			
100 $\mu\text{m}$	No data							
200 $\mu\text{m}$	2.13	2.20	123	126				

Various laser pulse shapes were applied in the experiments (see Fig. 141.43), including a 1-ns square pulse, a 1.4-ns shaped pulse consisting of a 0.5-ns, 3-TW power foot followed by a high-power ( $\sim 22$ -TW) plateau [see Fig. 141.43(a)], and a longer 1.8-ns shaped pulse with a 1-ns, low-power ( $\sim 2$ -TW) foot followed by a 0.8-ns, high-power square pulse [see Fig. 141.43(b)]. The low-intensity foot creates a plasma atmosphere around the target with which the high-intensity portion of the pulse interacts. This situation resembles the conditions of a shock-ignition target, where first a low-intensity pulse assembles the fuel and then at the end of the pulse, an intensity spike launches the ignitor shock wave into the shell. Figure 141.43(b) shows various versions of the 1.8-ns shaped pulse where the laser energy was varied between 13.6 to 27.1 kJ to irradiate targets with different on-target laser intensities, while keeping the intensity in the foot constant. The overlapping beam intensities in the peak reach up to  $\sim 6 \times 10^{15}$  W/cm<sup>2</sup> for the smallest target.

### 3. Diagnostics

The x-ray emission from the center of the target was measured temporally and spatially resolved using an x-ray framing camera (XRFC)<sup>27</sup> and temporally and spectrally resolved with a streaked x-ray spectrometer (SXS),<sup>28</sup> while time-integrated measurements of the x-ray emission in the  $\sim 3$ - to  $\sim 7$ -keV range were made with an x-ray microscope imager.<sup>33</sup> The XRFC used a  $4 \times 4$  array of 10- $\mu\text{m}$ -diam pinholes to produce 16 enlarged

images of the target on a microchannel-plate detector coupled to a charge-coupled-device camera. A 200- $\mu\text{m}$  Be foil and a thin (12- $\mu\text{m}$ ) Ti foil were placed in front of the detector. Combined with the spectral response of the diagnostic, this restricted the range of recorded x rays to  $\sim 3$  to 7 keV. An XRFC with a slow gating time of  $\sim 130$ -ps full width at half maximum (FWHM) was applied in the measurements. In some of the shots, a second faster ( $\sim 60$ -ps) XRFC was also used. The SXS employs a flat Bragg crystal in front of an x-ray streak camera for time-resolved, x-ray spectroscopy of laser-produced plasmas in the 1.4- to 20-keV photon-energy range. The SXS relies on a pinned mechanical reference system to create a discrete set of Bragg reflection geometries for a variety of crystals. For these experiments, a rubidium acid phthalate (RbAP) crystal dispersed the x rays in an energy range of 3.8 to 6.5 keV onto a 28-mm-long, 250- $\mu\text{m}$ -wide slit at the entrance of the streak camera, which was equipped with a photocathode comprised of a 12.5- $\mu\text{m}$ -thick Be foil coated with a thin 200-nm layer of KBr. A 127- $\mu\text{m}$ -thick Be blast filter protected the diagnostic from optical stray light and target debris.

The XRFC was absolutely timed with an accuracy of 50 ps through dedicated timing shots that used several laser beams to irradiate a 4-mm-diam plastic sphere coated with a thin layer of gold. The laser spots were spatially separated on target so that the generated x-ray emission was spatially separated and

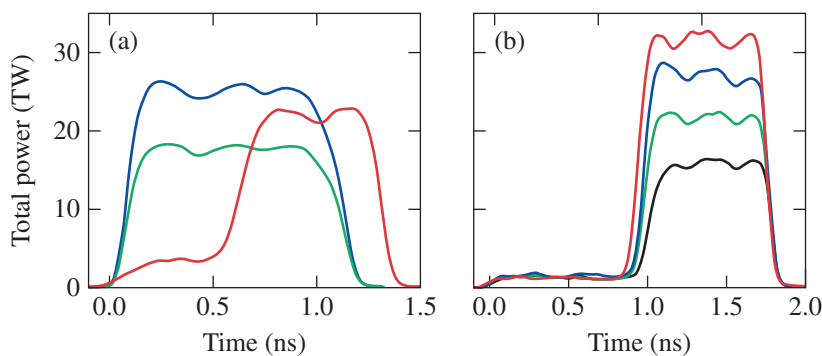


Figure 141.43

Total power of various laser pulse shapes that were used in the spherical strong-shock experiments. (a) Square pulse shapes (blue and green curves) with a pulse duration of 1 ns and shaped pulse (red curve) with a duration of 1.4 ns. (b) Shaped pulse with a 1-ns low-power foot followed by a 0.8-ns high-power square pulse. Various versions of this pulse form provide different laser energies on target while keeping the power in the foot constant.

E23754JR

unambiguously identified in the XRFC image. The timing of each laser beam was measured and cross-correlated with the measured time-resolved x-ray emission from each of the plasma spots. Details on the timing technique can be found in Ref. 34. In a similar way, the SXS diagnostic was also absolutely timed by using one laser beam interacting with a thin Ti foil and cross-correlating the x-ray emission with the laser pulse that generated the x-ray emission.

The hot electrons were characterized by measuring the hard x-ray emission in an energy range of 10 keV to  $\sim 700$  keV using several diagnostics simultaneously. A time-resolved, four-channel hard x-ray detector (HXRD)<sup>35</sup> provided a measurement of the time history of the hard x-ray emission and hot-electron temperature in the low-intensity shots. The HXRD diagnostic was affected by signal saturation in the high-intensity shots. Each channel of the HXRD system consists of a fast scintillator coupled to a fast microchannel plate/photomultiplier tube and is filtered by a combination of Al and Cu foils of different thicknesses, giving various cutoff energies in a range from  $\sim 20$  to 80 keV for the different channels. The time resolution of the HXRD system is  $\sim 100$  ps. Two time-integrated imaging-plate diagnostics—high-energy radiography imager (HERIE)<sup>36</sup> and bremsstrahlung x-ray spectrometer (BMXS)<sup>37</sup>—provided temperature and hot-electron fraction measurements on all shots. The BMXS spectrometer contains 13 filters of increasing Z from Al to Pb and then increasing thicknesses of Pb for differential filtering and Fuji BAS-MS image plates sandwiched between the filters as detectors. The image plates and filters are contained in a thick Pb box that shields hard x rays with energy of up to 2 MeV. A 12.5-cm-long Pb collimator with a 1.2-cm-diam hole suppresses background radiation from the vacuum chamber walls and other diagnostics. Details on the BMXS diagnostic and the data analysis can be found in Ref. 37. The HERIE diagnostic contains a large image plate inside a thick Pb box. A mask with nine small windows is placed in front of the image plate. Different filter materials were mounted in the windows to obtain the differential filtering. BMXS and HERIE cover spectral ranges from  $\sim 10$  to  $\sim 700$  keV and  $\sim 20$  to  $\sim 200$  keV, respectively, which is sufficient for the expected hot-electron temperatures of up to 100 keV. Because of the large dynamic range of the image plates, the two time-integrated diagnostics provided reliable measurements even for the highest laser intensity.

The laser light that reflected back from the target was measured from two adjacent beam ports (30 and 25), which were equipped with a full-aperture backscatter station (FABS),<sup>16,18</sup> providing spectrally resolved measurements of the backscattered light. Time-resolved spectra were recorded by several

streaked spectrometers covering the wavelength ranges of  $351 \pm 3$  nm for SBS,  $\sim 500$  to  $\sim 700$  nm for SRS, and  $234 \pm 4$  nm for  $3\omega/2$  emission from the TPD instability. In addition, several scatter calorimeters and FABS's provided time-resolved measurements of the fraction of absorbed laser power.<sup>16</sup>

## Experimental Results

### 1. X-Ray Emission Measurements

The SXS diagnostic provides a streaked x-ray spectrum showing, early in time, the x-ray emission from the interaction of the laser pulse with the plasma corona and, later in time, the x-ray flash from the shock convergence in the target center. Figure 141.44(a) shows an example of the SXS data from a target that was irradiated with a 1-ns square pulse; Fig. 141.44(b) shows a lineout along the time axis at the Ti He $_{\alpha}$ -emission wavelength

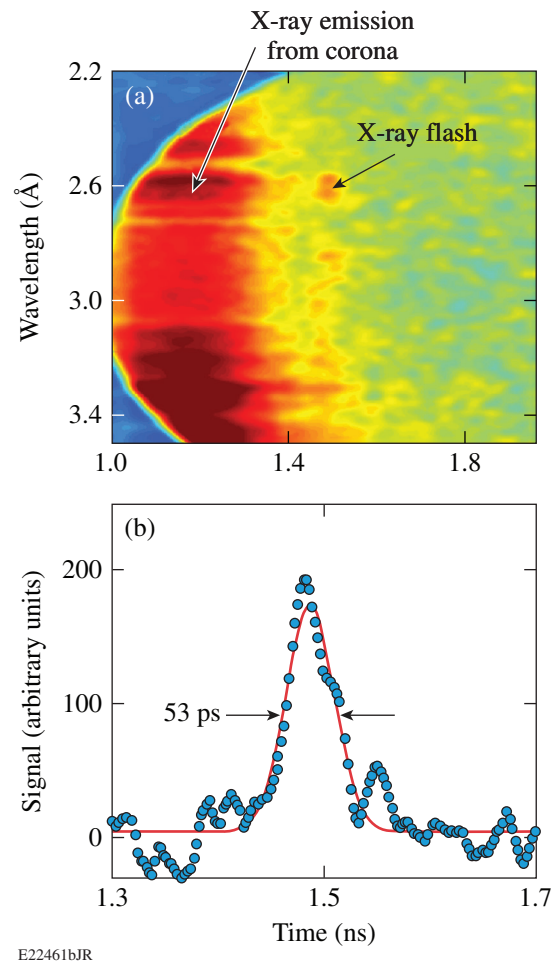


Figure 141.44

(a) Streaked x-ray spectrum showing, early in time, the x-ray emission from the plasma corona and, at 1.5 ns, the x-ray flash from the shock convergence. The target was irradiated with a 1-ns square pulse. (b) Time lineout at 2.6 Å of the x-ray flash with an emission time of 53 ps.

of  $\sim 2.6 \text{ \AA}$ . A short x-ray flash was measured with a FWHM emission time of 53 ps. By taking the temporal resolution of the instrument into account, this corresponds to a deconvolved emission time of  $\sim 35 \text{ ps}$ .

Figure 141.45 shows a portion of the raw data collected with the XRFC for a shot with a 1-ns square pulse. At early times, the observed x-ray emission originated from the hot corona when the laser was still interacting with the target. Although the laser pulse is nominally 1 ns long, the first image at 1.13 ns (Fig. 141.45) was taken when the laser was still on, as can be seen from the measured pulse shape in Fig. 141.43(a). As time

progressed and the laser shut off, the corona cooled and the x-ray emission from the target surface quickly disappeared. After a brief period where no x-ray emission was recorded, a small but bright source of x rays appeared at the target center, indicative of the shock convergence. Figure 141.46 renders a zoomed image of the emission from the center, demonstrating that the emission originated from a very small region. A diameter of  $15 \text{ }\mu\text{m}$  (FWHM) was measured, corresponding to a deconvolved size of  $\sim 9 \text{ }\mu\text{m}$  when taking the  $12\text{-}\mu\text{m}$  spatial resolution of the pinhole diagnostic into account. Measurements with the time-integrated x-ray microscope provided a higher spatial resolution ( $\sim 5 \text{ }\mu\text{m}$ ) and resulted in emission sizes of  $\sim 7 \text{ }\mu\text{m}$ .

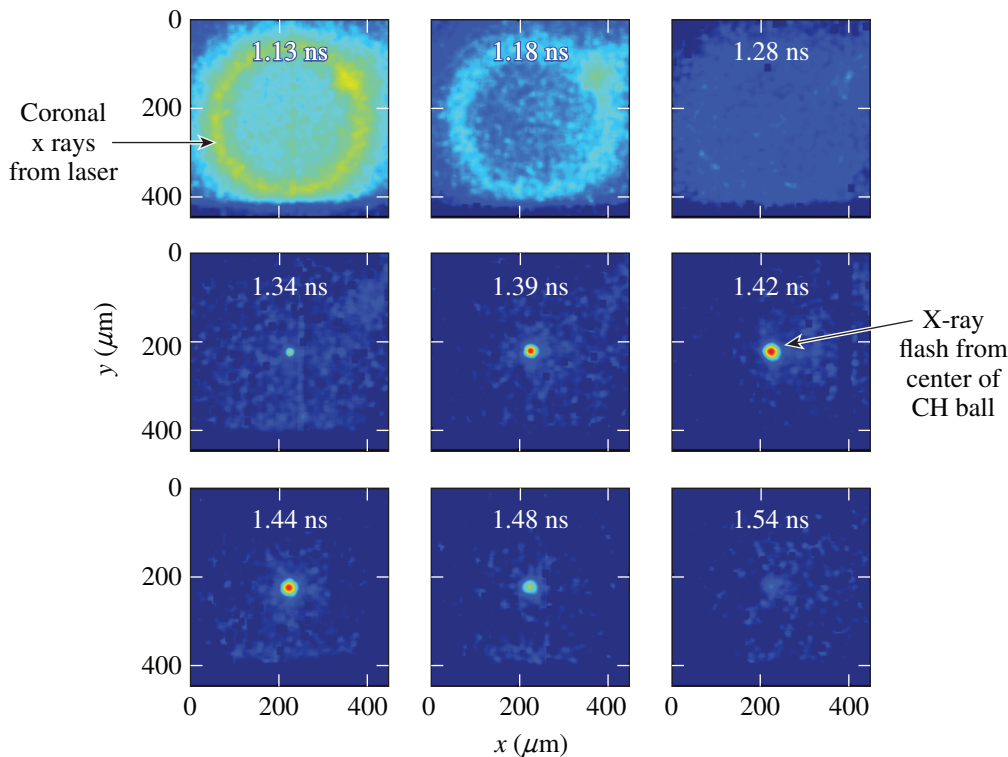


Figure 141.45 X-ray framing-camera images show the coronal x-ray emission from the target surface during the laser interaction and later the x-ray flash from the target center generated by the converged shock wave. The target was irradiated with a 1-ns square pulse.

E23233JR

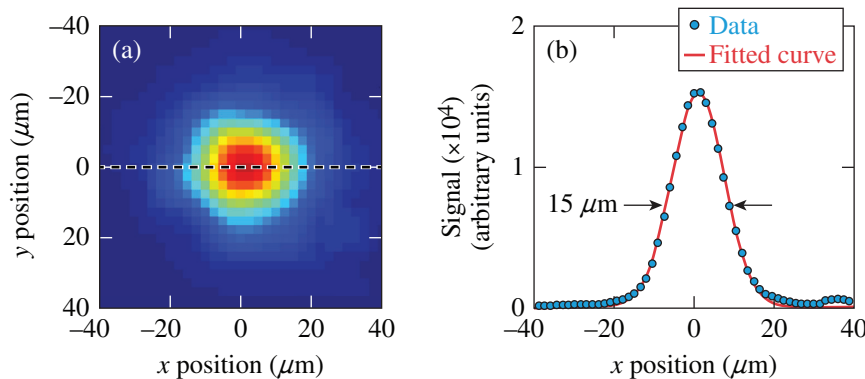


Figure 141.46 (a) Zoomed-in x-ray framing camera image of the emission from the target center at peak emission; (b) a horizontal lineout through the center of the emission, which is well fitted by a Gaussian profile with a width of  $15 \text{ }\mu\text{m}$ .

E22462cJR

Figure 141.47 shows the measured x-ray flash time obtained from the XRFC and SXS diagnostics as a function of the absorbed laser intensity, which is defined as the maximum calculated absorbed power divided by the calculated critical density surface area. The absorbed laser power is obtained from 1-D radiation–hydrodynamic simulations, which are in good agreement with measurements as shown in **Simulations** (p. 58). The temporal occurrence of the x-ray flash between the two diagnostics is within the absolute timing error of each other. With increasing intensity, an earlier flash time was measured, indicative of a stronger shock.

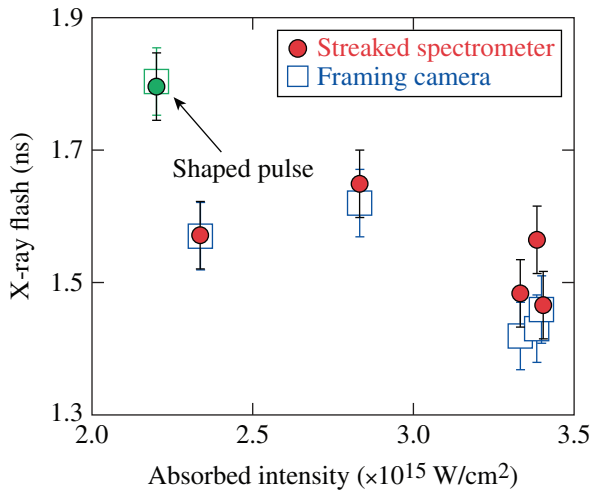


Figure 141.47

Measured x-ray flash time from the x-ray framing camera and streaked x-ray spectrometer versus absorbed laser intensity, which is defined as the maximum calculated absorbed power divided by the calculated critical-density surface area. The red symbols represent shots with the 1-ns square pulse, while the green symbol represents the 1.4-ns shaped pulse.

The strength of the measured x-ray signal from the target center depends on the laser intensity and, therefore, from the shock strength. Figure 141.48 shows the data from the time-integrating x-ray microscope using the 1.8-ns shaped pulse by varying the laser energy and the target diameter. The x-ray signal from the target center was integrated over the emission area and is shown as a function of the absorbed laser intensity. The open squares represent measurements with SSD and the solid dots are the results without SSD. The x-ray signal depends strongly on the laser intensity and SSD. The signal was measured at three different intensities without SSD and is seen to grow linearly with intensity, with the solid line being a linear fit through the no-SSD data. In addition, the signal increases significantly when switching SSD off,

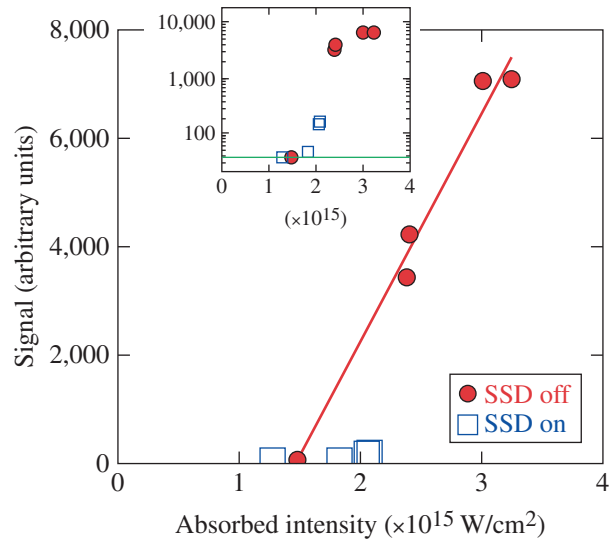


Figure 141.48

Measured time- and space-integrated x-ray emission from the target center as a function of the absorbed laser intensity. A time-integrating x-ray microscope<sup>33</sup> was used in this experiment. The square symbols represent measurements with smoothing by spectral dispersion (SSD) and the solid dots represent measurements without SSD. A shaped pulse with a pulse duration of 1.8 ns was used. The solid line is a linear fit to the dots. The inset shows the data in a semi-logarithmic plot with the noise floor given by the horizontal line.

with an  $\sim 25\times$ -higher signal at  $2.4 \times 10^{15}$  W/cm $^2$  and no SSD, compared to the measurement at  $2.1 \times 10^{15}$  W/cm $^2$  with SSD. By switching SSD off, more than a factor-of-2 additional hot electrons are generated (see **Hot-Electron Measurements** on p. 55). Both an increased intensity and more hot electrons clearly enhance the shock strength and the magnitude of the x-ray signal from shock convergence. It was mentioned in the previous section that the higher-than-expected concentration of Ti doping in the target resulted in the reabsorption of x-ray emission from the target center. To avoid the complication arising from opacity effects, we solely infer the shock strength from the measured time of the x-ray flash and not from the strength of the x-ray signal.

Experiments were performed with different-sized targets with and without SSD. Figure 141.49 shows the measured x-ray flash time as a function of the target diameter using the 1.8-ns shaped pulse. The x-ray flash is later for larger targets with a linear increase in flash time with diameter. Fitting lines through separate data with and without SSD show that for a fixed diameter, the flash appears  $\sim 90$  ps earlier when SSD is turned off. An earlier flash time indicates a stronger shock and is the result of the increased hot-electron production when SSD is turned off.

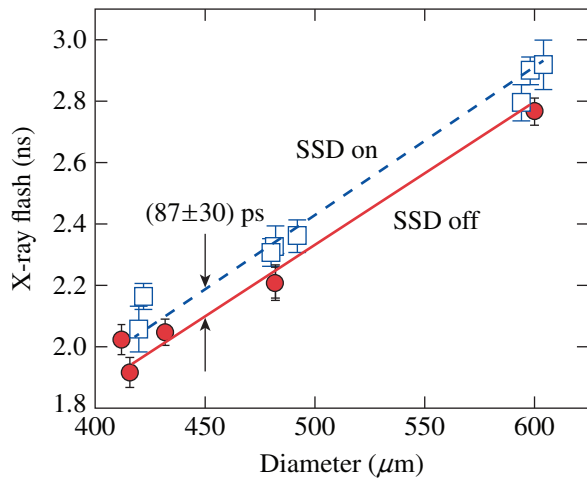


Figure 141.49  
 Measured x-ray flash time for different target sizes and shots with SSD (open squares) and without SSD (solid dots). The x-ray flash is later for larger targets and with SSD. An earlier flash time indicates a stronger shock. The 1.8-ns shaped pulse was used.

## 2. Hot-Electron Measurements

Laser-plasma instabilities can accelerate electrons to high energies, which can be detected via their hard x-ray bremsstrahlung emission when the electrons slow down in the target. The hard x-ray emission was measured with various diagnostics. Time-resolved measurements with HXRDI at lower laser intensities show that most of the electrons are generated in the second half of the high-intensity plateau of the shaped pulses. Unfortunately, HXRDI was driven into saturation at intensities above  $2 \times 10^{15}$  W/cm<sup>2</sup>, so no reliable time-resolved measurements are available for most of the shots. The time-integrated hot-electron fraction and the temperature were well characterized with the two diagnostics HERIE and BMXS, which provided data on all shots. Figures 141.50(a) and 141.50(b) show the measured hot-electron energy and hot-electron temperature, respectively, as functions of the incident laser energy. The average values of the energy and temperature of both diagnostics are shown. Measurements with and without SSD are represented by the squares and dots, respectively. The reason why most of the shots without SSD obtained higher laser energy lies in the fact that switching off the SSD modulation reduces the spectral bandwidth, which results in a slightly higher efficiency in frequency tripling. An attempt was made to reduce this energy in some of the shots without SSD so that a direct comparison of hot-electron production can be made at 24 kJ. Beside the slight increase in hot-electron energy with laser energy, the hot-electron fraction was more than doubled when SSD was turned off, reaching hot-electron energies of

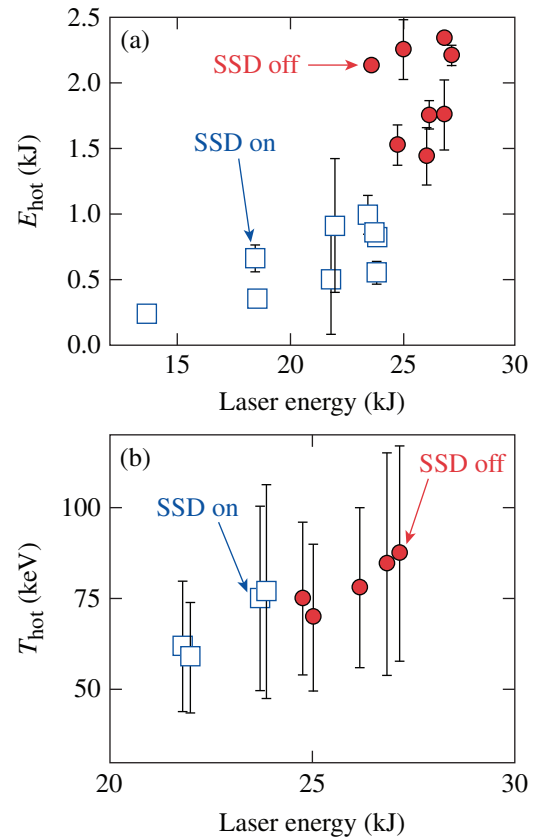


Figure 141.50  
 (a) Measured deposited hot-electron energy and (b) hot-electron temperature as a function of the incident laser energy. Measurements with and without SSD are represented by the squares and dots, respectively.

up to 2300 J being deposited into the solid target, which is up to 9% of the total laser energy.

The hot-electron energy increases only slightly with laser energy, indicating that an almost constant fraction of laser energy is converted into hot electrons. This indicates that the instabilities were driven highly into saturation. Previous experiments at lower laser intensity and larger density scale lengths<sup>38</sup> showed that the fraction of laser energy converted into hot electrons scaled exponentially with intensity from  $1.3$  to  $3 \times 10^{14}$  W/cm<sup>2</sup> and continued to grow at a slower rate above  $3 \times 10^{14}$  W/cm<sup>2</sup>, indicating the saturation of the instability. Other experiments<sup>17</sup> at shorter density scale lengths that extended up to  $\sim 2.5 \times 10^{15}$  W/cm<sup>2</sup> reported a similar trend of strong exponential increase in hot-electron production below  $1 \times 10^{15}$  W/cm<sup>2</sup> and a leveling off above  $1 \times 10^{15}$  W/cm<sup>2</sup>.

The measured bremsstrahlung emission was compared to Monte Carlo simulations assuming that the hot electrons were

generated isotropically within a  $180^\circ$  full divergence angle in the laser direction. The instantaneous conversion efficiency of laser power into hot-electron power reaches up to 15% in the second half of the high-intensity portion of the shaped laser pulse. The temperatures were inferred by fitting single-temperature Maxwellian distributions to the HERIE and BMXS data ranging from  $\sim 60$  to  $\sim 80$  keV, slightly increasing with higher laser energy. No significant difference in temperature was noted when SSD was turned off. The plotted temperatures are the average from both diagnostics with the error bars indicating the difference between both time-integrated diagnostics with BMXS measuring temperatures at the higher end and HERIE at the lower end.

### 3. Backscatter Measurements

Laser-plasma instabilities affect the laser-energy coupling and are sources for hot electrons and backscattered light. The optical signals from the laser backscatter diagnostics are compared for two laser shots: One shot with (shot 72676) and another without (shot 72678) SSD. Although shot 72678 had  $\sim 13\%$  higher energy (26.8 kJ) and accordingly higher incident laser intensity ( $4.4 \times 10^{15}$  W/cm $^2$ ) compared to shot 72676 (23.8 kJ,  $3.9 \times 10^{15}$  W/cm $^2$ ), the slight difference in laser intensity is an insignificant factor in explaining the difference in the LPI signatures. As a matter of fact, the optical emissions generated from SBS and TPD processes do not show any significant difference. Only the SRS-generated optical emission is very different and indicates a qualitative difference in the laser-plasma interaction when SSD is applied.

Figure 141.51 shows the reflected SBS spectra, for shots 72676 (SSD on) and 72678 (SSD off), which do not appear to be sensitive to the operation of SSD. The SBS signal exhibits a large spike as soon as the intensity spike is launched, which is caused by the local increase of the velocity gradient in the corona and a rapidly increasing ablation rate. During the short time interval of  $\sim 150$  ps, up to 15% of the laser energy is back-reflected. The amount of laser light scattered by SBS during the remainder of the main drive, however, is lower and results, over the entire pulse duration, in up to  $\sim 7\%$  of the laser energy. The near-backscattered light outside the FABS aperture was measured by the near-backscatter image (NBI) as well as by the scatter calorimeters (SCAL's). The overall laser-energy absorption was measured to be  $\sim 55\% \pm 5\%$  for all of the shots.

SRS drives electron plasma waves by scattering laser photons and transferring some fraction of the photon energy to the plasma waves; therefore, the SRS-scattered photons possess a longer wavelength than the incident laser wavelength. SRS is excited in a plasma region with electron densities below the

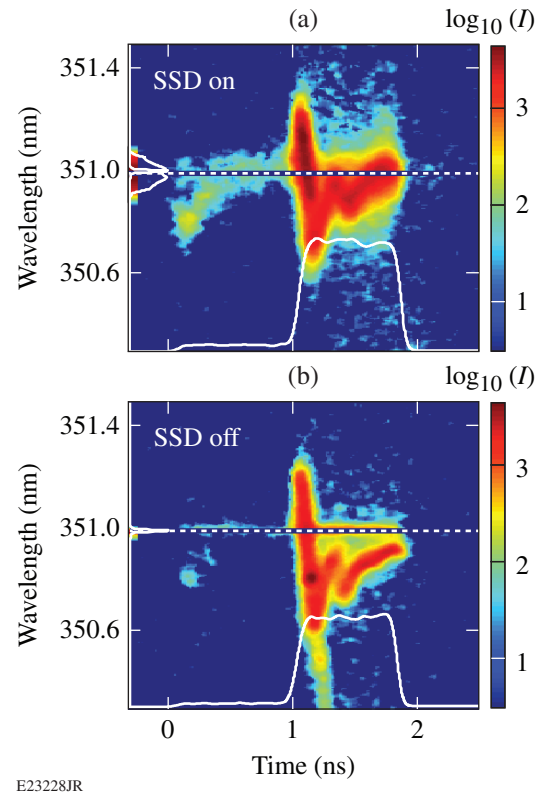


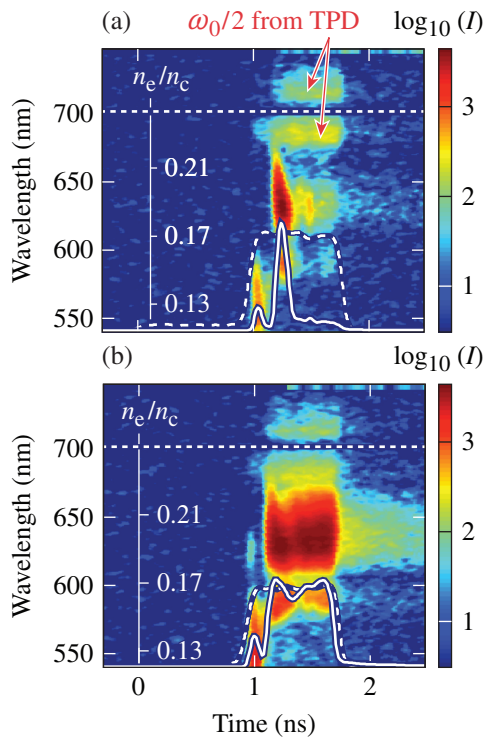
Figure 141.51

Streaked optical spectrographs measuring the stimulated Brillouin scattering (SBS) in one beam (Beam 30) (a) with SSD for shot 72676 and (b) without SSD for shot 72678. No significant difference in SBS is observed between SSD on and off. The intensity is rendered on a logarithmic scale. The y axis shows the wavelength of the reflected light and the x axis shows the time. The white curve represents the laser pulse shape.

quarter-critical density. The TPD process operates close to the quarter-critical density and converts an incident laser photon into two electron plasma waves that each carry about half of the photon energy.

The instabilities grow rapidly when a certain laser-intensity threshold is surpassed, which depends on the plasma density scale length and the electron temperature. This threshold from linear theory can be estimated for TPD with  $I_{\text{TPD}} \approx (8 \times T_{\text{keV}} / L_{\mu} \lambda_{\mu}) \times 10^{15}$  W/cm $^2$  (Ref. 39), where  $T_{\text{keV}}$ ,  $L_{\mu}$ , and  $\lambda_{\mu}$  are the electron temperature in keV, the density scale length in  $\mu\text{m}$ , and the laser wavelength in  $\mu\text{m}$ , respectively. For SRS, the threshold at  $\sim n_c/4$  is estimated by  $I_{\text{SRS}} \approx (5 \times T_{\text{keV}} / L_{\mu}^{4/3} \lambda_{\mu}^{2/3}) \times 10^{16}$  W/cm $^2$  (Ref. 40). *LILAC* simulations predict  $T_{\text{keV}} \approx 3.5$  and  $L_{\mu} \approx 120$  during the high-intensity portion of the laser pulse at quarter-critical density, which results in a threshold of  $\sim 7 \times 10^{14}$  W/cm $^2$  for both TPD and SRS. The threshold is exceeded during the rise of the high-intensity portion of the laser pulse.

Figure 141.52(a) shows a streaked optical spectrograph of the SRS back-reflected light when SSD was turned on, while Fig. 141.52(b) shows the result with no SSD. When the laser pulse (dashed curve) rises to its maximum intensity, SRS is excited  $\sim 100$  ps after the strong shock is launched in a short burst of signal in the wavelength range of 540 to 600 nm, followed by a second burst at longer wavelengths ( $\sim 600$  to 660 nm) [see Fig. 141.52(a)]. The wavelength of the backscattered light correlates with the electron density of the plasma region from where the SRS signal was generated. A longer wavelength corresponds to a higher density as indicated by the white scale. The white curve is the spectrally integrated signal from  $\sim 540$  to 660 nm and represents the temporal evolution of the SRS signal. The SRS signal is strongly quenched in the second half of the high-intensity plateau. The situation was completely different when SSD was turned off, which is shown in Fig. 141.52(b). The SRS signal was not quenched and persisted over the whole

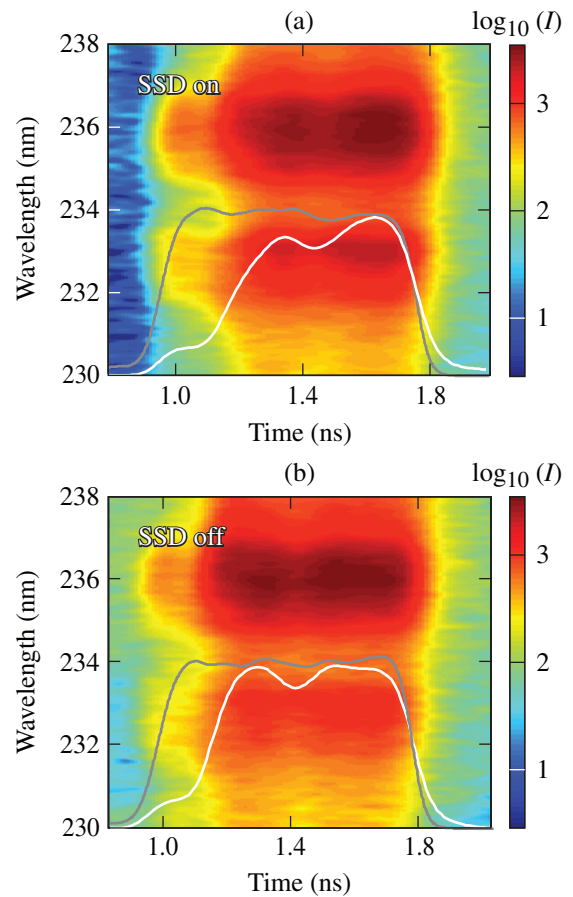


E23226aJR

Figure 141.52  
Streaked optical spectrographs measuring the stimulated Raman scattering (SRS) back-scattered signal in one beam (Beam 30) (a) with SSD for shot 72676 and (b) without SSD for shot 72678. The white dashed curve depicts the laser pulse shape and the white solid curve depicts the spectrally averaged SRS signal in arbitrary units. The white scale relates the wavelength to the electron density from where in the plasma the SRS signal was generated. A  $5\times$  higher SRS signal is generated without SSD.

duration of the high-intensity plateau. The temporal integrations of the white curves show that with SSD off, a factor-of-5-more SRS-backscattered signal was produced compared to the case with SSD. This is accompanied with a significant increase in hot-electron production as discussed in **Hot-Electron Measurements** (p. 55).

The two emission lobes at  $\sim 700$  nm that persisted over the whole duration of the high-intensity plateau were optical emission generated by electron plasma waves with half the laser frequency ( $\omega_0/2$ ) caused by TPD. Similarly, the  $3\omega_0/2$  emission, which is also a signature optical emission from TPD,<sup>17</sup> carried on over the duration of the high-intensity plateau and was unaffected by SSD (see Fig. 141.53).



E23227aJR

Figure 141.53  
Streaked optical spectrographs measuring the  $3\omega_0/2$  emission signal generated by the two-plasmon–decay (TPD) instability in one beam (Beam 30) (a) with SSD for shot 72676 and (b) without SSD for shot 72678. No significant difference in TPD activity is observed between the shots with and without SSD. The gray curve shows part of the laser pulse and the white curve represents the spectrally integrated  $3\omega_0/2$  emission.

Previous experiments on the 24-beam OMEGA laser studied TPD and SRS with distributed phase plates (DPP's) and with and without SSD using laser intensities of up to  $\sim 1 \times 10^{15}$  W/cm<sup>2</sup> but longer density scale length ( $\sim 800$   $\mu$ m) and lower temperatures ( $\sim 1$  keV) (Ref. 41). A strong reduction (three orders of magnitude) of SRS was observed when SSD modulation was switched on, but SSD affected TPD only slightly. Quantitative differences remain, however, which are probably a consequence of the different plasma conditions; this is very similar to the observations made in our experiment. SSD reduced SRS backscatter by a factor of  $\sim 5$  while hardly affecting TPD. The inverse growth rates of SRS and TPD are of the order of subpicoseconds and are much shorter than the smoothing time provided by SSD, which is  $\sim 25$  to  $50$  ps for 1-THz bandwidth.<sup>42</sup> Therefore, it is not expected that SSD directly disrupts the growth of these laser–plasma instabilities. The suppression of beam filamentation with SSD might be one mechanism for the reduction in SRS. Previous experiments<sup>43</sup> reported a correlation between the onset of beam filamentation and the appearance of SBS and SRS emission in a laser beam that was not optically smoothed. When the laser beam was optically smoothed it did not break up in filaments and SRS and SBS were substantially suppressed.

Our data indicate that although the TPD instability is excited, SRS appears to be the primary generation mechanism of hot electrons. The observation of moderate hot-electron temperatures at these laser intensities has a significant impact on SI designs since they can enhance the ignitor shock<sup>44</sup> and improve the implosion performance.<sup>12</sup>

### Simulations

The shock and ablation pressures, inferred from one-dimensional (1-D) radiation–hydrodynamic simulations with the code *LILAC*,<sup>45</sup> were constrained by the experimental observables. The timing of the x-ray emission from the center was the primary constraint. The measured hot-electron fraction and temperature were used as input in the simulations as well as the temporal dependence of the hot-electron production, which was assumed to be the same for all shots. Details on the simulations can be found in Ref. 22. As an example, Fig. 141.54 shows the observed (solid) and simulated (dashed) quantities for one shot. The gray curve represents the incident laser power and the blue curves represent the absorbed laser power, showing agreement between measurement and simulation. The red curves show the temporal evolution of the hard x-ray emission. The solid red curve represents the measurement and the dashed red curve represents the simulated hard x-ray emission, reflecting the time-dependent generation of the hot

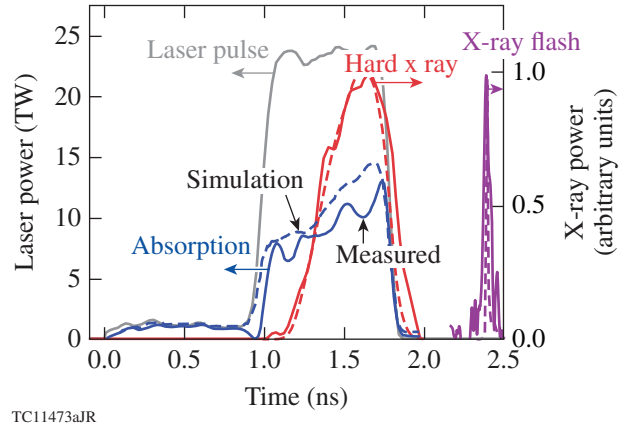
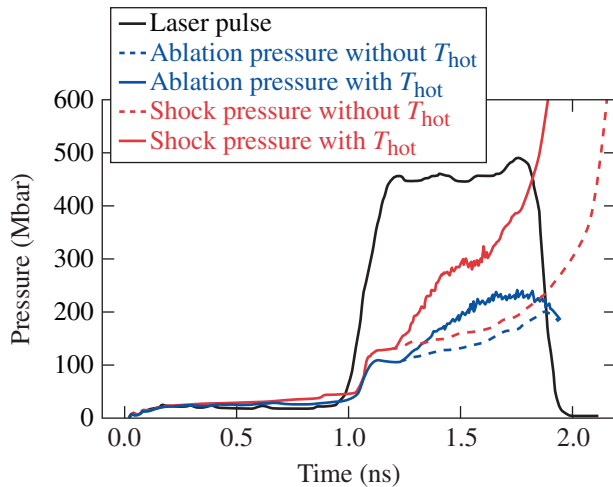


Figure 141.54

Comparison of measured (solid curves) and simulated (dashed curves) quantities for absorbed laser power (blue), hard x-ray emission  $>50$  keV (red), and x-ray emission from the center of the target (magenta). The 1-D hydrodynamic simulations are constrained by the experimental observables.

electrons. The magenta lines show the x-ray flash from the target center. The simulations employed a multigroup radiation diffusion model, equation-of-state (EOS) models based on Thomas–Fermi<sup>46</sup> or *SESAME*<sup>47,48</sup> flux-limited thermal transport,<sup>49</sup> and a hot-electron transport package.<sup>45,50</sup> A fraction of the laser energy reaching the quarter-critical surface is converted into hot electrons, assuming a single-temperature Maxwellian distribution and an isotropic emission within a full  $180^\circ$  divergence angle in the forward direction. The hot electrons are transported in a straight line into the target. The transport of the thermal electrons is described by a flux limiter, which is the only free parameter in the simulations. It is adjusted to match the experimentally measured x-ray flash time and varies between 5% and 8%. The ablation pressure is the pressure in the shell at the position where the material velocity is zero in the lab frame. Although this is an approximate definition of the ablation surface, it is computationally the most accurate and is quite robust for targets that are converging with small fluid velocities ( $<10^7$  cm/s) such as the solid spheres in our experiments.

Figure 141.55 shows the temporal evolution of the inferred shock and ablation pressures for one laser shot and two simulations with and without hot electrons. The black curve indicates the laser power in arbitrary units. The ablation pressure (blue curves) increases as a function of time and reaches up to  $\sim 220$  Mbar at  $\sim 1.7$  ns (solid blue curve) when hot electrons are included in the simulations. The pressure is built up from both thermal conduction of the absorbed laser energy and the energy deposition by hot electrons. The hot-electron contribution to



E23271aJR

Figure 141.55

Temporal evolution of the simulated ablation (blue) and shock pressures (red) with (solid curves) and without (dashed curves) hot electrons.

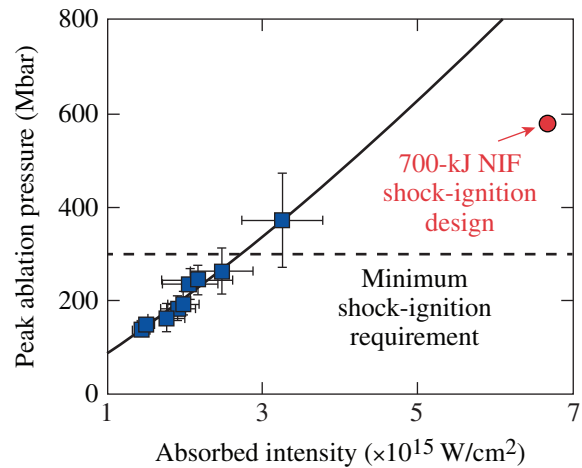
the ablation pressure is  $\sim 30\%$ , inferred by comparing it to a simulation that neglected the hot-electron contribution (dashed curve). It should be pointed out that the simulation without hot electrons calculates a later flash time than measured. The shock pressure without hot electrons (dashed red curve) closely follows the ablation pressure and rapidly increases in time because of convergence effects after the laser pulse is turned off.<sup>24</sup> The shock pressure including hot electrons exceeds 300 Mbar at 1.7 ns (solid red curve). The shock pressure is even more enhanced by hot electrons compared to the ablation pressure. The increase reaches  $\sim 50\%$  when compared to the simulation without hot electrons. A higher fraction of the hot electrons is absorbed in the target volume behind the ablation surface, further augmenting the shock formation, while a smaller fraction is absorbed in front of the ablation surface. Similar conclusions were drawn from recent theoretical work showing that it should be possible to generate  $\sim 300$ -Mbar shock pressures resulting solely from hot electrons,<sup>51,52</sup> which might open a path to ignition based entirely on hot electrons.<sup>53</sup>

### Discussion

The shock and ablation pressures are inferred by constraining radiation–hydrodynamic simulations to the experimental observables: the temporal occurrence of the x-ray emission, the hot-electron energy and temperature distribution, and the temporal evolution of the hard x-ray emission. In the SSS experiments, the distance from the quarter-critical density up to the ablation surface is typically  $\sim 120 \mu\text{m}$  during the later part of the intensity spike. The spatial integration of the density profile in this region results in areal densities of  $\sim 1 \text{ mg/cm}^2$ , which

provides only minimal stopping power for the hot electrons in the material before the ablation front compared to the areal density ( $\sim 20 \text{ mg/cm}^2$ ) in the solid-density material behind the ablation front up to the shock front. Consequently, most of the hot electrons deposit their energy behind the ablation front, which affects the partition of the pressures at the ablation surface and the shock front. The hot electrons, therefore, enhance the shock strength beyond the applied ablation pressure, which explains why the hot electrons enhance the shock pressure more than the ablation pressure (see Fig. 141.55). For the shock it is subordinate how the energy was provided, whether from absorbed hot electrons or via thermal heat conduction between the critical density to the ablation surface or a combination of both mechanisms. Therefore, whether the shock is solely driven by the rocket effect or by a combination of ablation pressure and hot-electron energy, the pressure behind the shock must be independent of the mechanism driving the shock and even insensitive to many physics details. To support this point we applied different EOS models in the simulations. Thomas–Fermi or *SESAME* EOS models result in essentially the same shock pressure and reproduce the experimental observables although differences in the post-shock mass-density distribution are observed.

Figure 141.56 shows the scaling of the maximum ablation pressure versus the absorbed laser intensity. The error bars reflect the uncertainty in the simulated pressures and the calcu-



E23581JR

Figure 141.56

Scaling of the inferred maximum ablation pressure versus the absorbed laser intensity. The ablation pressures (solid squares) were inferred from simulations that match all the experimental observables. The solid line shows the extrapolation to higher intensities based on the OMEGA experiments, which is favorable for shock ignition. The solid red circle indicates the requirement for the 700-kJ NIF shock-ignition design.<sup>12</sup>

lated absorbed laser intensities based on the absolute measurement uncertainty in the x-ray flash time ( $\pm 50$  ps). Hot electrons significantly contribute to the shock formation and increase the ablation pressure by  $\sim 30\%$ . At the highest absorbed intensity, the minimum required ablation pressure of 300 Mbar for shock-ignition designs is clearly surpassed. The solid line shows the extrapolation to higher intensities based on the OMEGA experiments, which is favorable for shock ignition. The solid red circle denotes the required ablation pressure for the 700-kJ NIF shock-ignition design presented in Ref. 12. Based on this extrapolation, ablation pressures exceeding 800 Mbar are expected at absorbed intensities of  $6 \times 10^{15}$  W/cm<sup>2</sup>, which would exceed the required 600 Mbar by  $\sim 30\%$ . The current OMEGA experiments were conducted, however, at a shorter density scale length—about a factor of 3 shorter than required for the 700-kJ NIF shock-ignition design. Further experiments on the NIF are required to study the ablation-pressure scaling for longer density scale length.

In summary, peak ablation pressures of close to  $\sim 400$  Mbar have been produced on OMEGA using small solid spherical targets that were irradiated at high incident laser intensities (up to  $6 \times 10^{15}$  W/cm<sup>2</sup>) in a regime that is relevant for shock ignition. The strength of the shocks was assessed using the timing of the x-ray flash produced from the shock convergence at the target center. Large amounts of hot electrons were produced that deposited their energy (up to 2.3 kJ) in the target and significantly enhanced (by up to  $\sim 50\%$ ) the shock strength. Measurements of the timing and magnitude of the x-ray flash and the hot-electron fraction demonstrate the enhancement of the shock strength from hot electrons. The extrapolation of the OMEGA results to the condition required for shock ignition on the NIF looks promising. The experiments also open the way to develop a platform to study material properties under extreme pressures by placing materials of interest at the center of the plastic sphere and compressing the sample material to Gbar pressures by the convergent shock.

#### ACKNOWLEDGMENT

This material is based upon work supported by the Department of Energy National Nuclear Security Administration under Award Number DE-NA0001944, the OFES Fusion Science Center grant No. DE-FC02-04ER54789, the DOE Laboratory Basic Science Program, the University of Rochester, and the New York State Energy Research and Development Authority. The support of DOE does not constitute an endorsement by DOE of the views expressed in this article.

#### REFERENCES

1. R. Betti, C. D. Zhou, K. S. Anderson, L. J. Perkins, W. Theobald, and A. A. Solodov, *Phys. Rev. Lett.* **98**, 155001 (2007).

2. W. Theobald, R. Betti, C. Stoeckl, K. S. Anderson, J. A. Delettrez, V. Yu. Glebov, V. N. Goncharov, F. J. Marshall, D. N. Maywar, R. L. McCrory, D. D. Meyerhofer, P. B. Radha, T. C. Sangster, W. Seka, D. Shvarts, V. A. Smalyuk, A. A. Solodov, B. Yaakobi, C. D. Zhou, J. A. Frenje, C. K. Li, F. H. Séguin, R. D. Petrasso, and L. J. Perkins, *Phys. Plasmas* **15**, 056306 (2008).
3. L. J. Perkins, R. Betti, K. N. LaFortune, and W. H. Williams, *Phys. Rev. Lett.* **103**, 045004 (2009).
4. X. Ribeyre, G. Schurtz, M. Lafon, S. Galera, and S. Weber, *Plasma Phys. Control. Fusion* **51**, 015013 (2009).
5. S. Atzeni, X. Ribeyre, G. Schurtz, A. J. Schmitt, B. Canaud, R. Betti, and L. J. Perkins, *Nucl. Fusion* **54**, 054008 (2014).
6. J. Nuckolls *et al.*, *Nature* **239**, 139 (1972).
7. J. D. Lindl, *Inertial Confinement Fusion: The Quest for Ignition and Energy Gain Using Indirect Drive* (Springer-Verlag, New York, 1998).
8. V. A. Shcherbakov, *Sov. J. Plasma Phys.* **9**, 240 (1983).
9. A. J. Schmitt *et al.*, *Phys. Plasmas* **17**, 042701 (2010).
10. D. Batani, S. Baton, A. Casner, S. Depierreux, M. Hohenberger, O. Klimo, M. Koenig, C. Labaune, X. Ribeyre, C. Rousseaux, G. Schurtz, W. Theobald, and V. T. Tikhonchuk, *Nucl. Fusion* **54**, 054009 (2014).
11. S. Atzeni and J. Meyer-ter-Vehn, *The Physics of Inertial Fusion: Beam Plasma Interaction, Hydrodynamics, Hot Dense Matter*, International Series of Monographs on Physics (Clarendon Press, Oxford, 2004).
12. K. S. Anderson, R. Betti, P. W. McKenty, T. J. B. Collins, M. Hohenberger, W. Theobald, R. S. Craxton, J. A. Delettrez, M. Lafon, J. A. Marozas, R. Nora, S. Skupsky, and A. Shvydky, *Phys. Plasmas* **20**, 056312 (2013).
13. W. L. Kruer, in *The Physics of Laser Plasma Interactions*, Frontiers in Physics, Vol. 73, edited by D. Pines (Addison-Wesley, Redwood City, CA, 1988).
14. A. A. Offenberger *et al.*, *J. Appl. Phys.* **47**, 1451 (1976).
15. W. Seka, H. A. Baldis, J. Fuchs, S. P. Regan, D. D. Meyerhofer, C. Stoeckl, B. Yaakobi, R. S. Craxton, and R. W. Short, *Phys. Rev. Lett.* **89**, 175002 (2002).
16. S. P. Regan, D. K. Bradley, A. V. Chirikikh, R. S. Craxton, D. D. Meyerhofer, W. Seka, R. W. Short, A. Simon, R. P. J. Town, B. Yaakobi, J. J. Carroll III, and R. P. Drake, *Phys. Plasmas* **6**, 2072 (1999).
17. C. Stoeckl, R. E. Bahr, B. Yaakobi, W. Seka, S. P. Regan, R. S. Craxton, J. A. Delettrez, R. W. Short, J. Myatt, A. V. Maximov, and H. Baldis, *Phys. Rev. Lett.* **90**, 235002 (2003).
18. W. Seka, D. H. Edgell, J. F. Myatt, A. V. Maximov, R. W. Short, V. N. Goncharov, and H. A. Baldis, *Phys. Plasmas* **16**, 052701 (2009).
19. S. D. Baton *et al.*, *Phys. Rev. Lett.* **108**, 195002 (2012).
20. M. Hohenberger, W. Theobald, S. X. Hu, K. S. Anderson, R. Betti, T. R. Boehly, A. Casner, D. E. Fratanduono, M. Lafon, D. D. Meyerhofer,

- R. Nora, X. Ribeyre, T. C. Sangster, G. Schurtz, W. Seka, C. Stoeckl, and B. Yaakobi, *Phys. Plasmas* **21**, 022702 (2014).
21. D. Batani *et al.*, *Phys. Plasmas* **21**, 032710 (2014).
  22. R. Nora, W. Theobald, R. Betti, F. J. Marshall, D. T. Michel, W. Seka, B. Yaakobi, M. Lafon, C. Stoeckl, J. A. Delettrez, A. A. Solodov, A. Casner, C. Reverdin, X. Ribeyre, A. Vallet, J. Peebles, F. N. Beg, and M. S. Wei, *Phys. Rev. Lett.* **114**, 045001 (2015).
  23. G. H. Miller, E. I. Moses, and C. R. Wuest, *Opt. Eng.* **43**, 2841 (2004).
  24. G. Guderley, *Luftfahrtforschung* **19**, 302 (1942).
  25. A. L. Kritcher *et al.*, *High Energy Density Phys.* **10**, 27 (2014).
  26. T. R. Boehly, D. L. Brown, R. S. Craxton, R. L. Keck, J. P. Knauer, J. H. Kelly, T. J. Kessler, S. A. Kumpan, S. J. Loucks, S. A. Letzring, F. J. Marshall, R. L. McCrory, S. F. B. Morse, W. Seka, J. M. Soures, and C. P. Verdon, *Opt. Commun.* **133**, 495 (1997).
  27. D. K. Bradley, P. M. Bell, J. D. Kilkenny, R. Hanks, O. Landen, P. A. Jaanimagi, P. W. McKenty, and C. P. Verdon, *Rev. Sci. Instrum.* **63**, 4813 (1992).
  28. M. Millecchia, S. P. Regan, R. E. Bahr, M. Romanofsky, and C. Sorce, *Rev. Sci. Instrum.* **83**, 10E107 (2012).
  29. S. P. Regan, T. C. Sangster, D. D. Meyerhofer, W. Seka, R. Epstein, S. J. Loucks, R. L. McCrory, C. Stoeckl, V. Yu. Glebov, O. S. Jones, D. A. Callahan, P. A. Amendt, N. B. Meezan, L. J. Suter, M. D. Rosen, O. L. Landen, E. L. DeWald, S. H. Glenzer, C. Sorce, S. Dixit, R. E. Turner, and B. MacGowan, *J. Phys.: Conf. Ser.* **112**, 022077 (2008).
  30. T. R. Boehly, V. A. Smalyuk, D. D. Meyerhofer, J. P. Knauer, D. K. Bradley, R. S. Craxton, M. J. Guardalben, S. Skupsky, and T. J. Kessler, *J. Appl. Phys.* **85**, 3444 (1999).
  31. S. Skupsky, R. W. Short, T. Kessler, R. S. Craxton, S. Letzring, and J. M. Soures, *J. Appl. Phys.* **66**, 3456 (1989).
  32. S. P. Regan, J. A. Marozas, J. H. Kelly, T. R. Boehly, W. R. Donaldson, P. A. Jaanimagi, R. L. Keck, T. J. Kessler, D. D. Meyerhofer, W. Seka, S. Skupsky, and V. A. Smalyuk, *J. Opt. Soc. Am. B* **17**, 1483 (2000).
  33. F. J. Marshall and J. A. Oertel, *Rev. Sci. Instrum.* **68**, 735 (1997).
  34. D. T. Michel, V. N. Goncharov, I. V. Igumenshchev, R. Epstein, and D. H. Froula, *Phys. Rev. Lett.* **111**, 245005 (2013).
  35. C. Stoeckl, V. Yu. Glebov, D. D. Meyerhofer, W. Seka, B. Yaakobi, R. P. J. Town, and J. D. Zuegel, *Rev. Sci. Instrum.* **72**, 1197 (2001).
  36. R. Tommasini, J. A. Koch, N. Izumi, L. A. Welsler, R. C. Mancini, J. Delettrez, S. Regan, and V. Smalyuk, *Rev. Sci. Instrum.* **77**, 10E303 (2006).
  37. C. D. Chen *et al.*, *Rev. Sci. Instrum.* **79**, 10E305 (2008).
  38. D. H. Froula, B. Yaakobi, S. X. Hu, P.-Y. Chang, R. S. Craxton, D. H. Edgell, R. Follett, D. T. Michel, J. F. Myatt, W. Seka, R. W. Short, A. Solodov, and C. Stoeckl, *Phys. Rev. Lett.* **108**, 165003 (2012).
  39. A. Simon, R. W. Short, E. A. Williams, and T. Dewandre, *Phys. Fluids* **26**, 3107 (1983).
  40. H. A. Baldis, E. M. Campbell, and W. L. Kruer, in *Handbook of Plasma Physics*, edited by M. N. Rosenbluth and R. Z. Sagdeev, Vol. 3: Physics of Laser Plasma, edited by A. Rubenchik and S. Witkowski (North-Holland, Amsterdam, 1991).
  41. W. Seka, R. E. Bahr, R. W. Short, A. Simon, R. S. Craxton, D. S. Montgomery, and A. E. Rubenchik, *Phys. Fluids B* **4**, 2232 (1992).
  42. *LLE Review Quarterly Report* **36**, 158, Laboratory for Laser Energetics, University of Rochester, Rochester, NY, LLE Document No. DOE/DP/40200-79 (1988).
  43. O. Willi *et al.*, *Phys. Fluids B* **2**, 1318 (1990).
  44. R. Betti, W. Theobald, C. D. Zhou, K. S. Anderson, P. W. McKenty, S. Skupsky, D. Shvarts, V. N. Goncharov, J. A. Delettrez, P. B. Radha, T. C. Sangster, C. Stoeckl, and D. D. Meyerhofer, *J. Phys.: Conf. Ser.* **112**, 022024 (2008).
  45. J. Delettrez and E. B. Goldman, Laboratory for Laser Energetics, University of Rochester, Rochester, NY, LLE Report No. 36 (1976).
  46. A. R. Bell, Rutherford Appleton Laboratory, Chilton, Didcot, Oxon, England, Report RL-80-091 (1980).
  47. G. I. Kerley, *Phys. Earth Planet. Inter.* **6**, 78 (1972).
  48. G. I. Kerley, Sandia National Laboratory, Albuquerque, NM, Report SAND2003-3613 (2003).
  49. R. C. Malone, R. L. McCrory, and R. L. Morse, *Phys. Rev. Lett.* **34**, 721 (1975).
  50. J. Delettrez, R. Epstein, M. C. Richardson, P. A. Jaanimagi, and B. L. Henke, *Phys. Rev. A* **36**, 3926 (1987); M. C. Richardson, P. W. McKenty, F. J. Marshall, C. P. Verdon, J. M. Soures, R. L. McCrory, O. Barnouin, R. S. Craxton, J. Delettrez, R. L. Hutchison, P. A. Jaanimagi, R. Keck, T. Kessler, H. Kim, S. A. Letzring, D. M. Roback, W. Seka, S. Skupsky, B. Yaakobi, S. M. Lane, and S. Prussin, in *Laser Interaction and Related Plasma Phenomena*, edited by H. Hora and G. H. Miley (Plenum Publishing, New York, 1986), Vol. 7, pp. 421–448.
  51. S. Gus'kov *et al.*, *Phys. Rev. Lett.* **109**, 255004 (2012).
  52. X. Ribeyre *et al.*, *Phys. Plasmas* **20**, 062705 (2013).
  53. R. Betti, R. Nora, K. S. Anderson, M. Lafon, W. Theobald, R. Yan, and C. Ren, *Bull. Am. Phys. Soc.* **58**, 31 (2013).